

# Interpretable Safety Alignment via SAE-Constructed Low-Rank Subspace Adaptation

Dianyun Wang\* Qingsen Ma\* Yuhu Shang\* Zhifeng Lu\*

Lechen Ning Zhenbo Xu Huijia Wu<sup>†</sup> Zhaofeng He

Beijing University of Posts and Telecommunications, Beijing, China

\*Equal contribution <sup>†</sup>Corresponding author

## Abstract

Parameter-efficient fine-tuning has become the dominant paradigm for adapting large language models to downstream tasks. Low-rank adaptation methods such as LoRA operate under the assumption that task-relevant weight updates reside in a low-rank subspace, yet this subspace is learned implicitly from data in a black-box manner, offering no interpretability or direct control. We hypothesize that this difficulty stems from polysemy—individual dimensions encoding multiple entangled concepts. To address this, we leverage pre-trained Sparse Autoencoders (SAEs) to identify task-relevant features in a disentangled feature space, then construct an explicit, interpretable low-rank subspace to guide adapter initialization. We provide theoretical analysis proving that under monosemanticity assumptions, SAE-based subspace identification achieves arbitrarily small recovery error, while direct identification in polysemantic space suffers an irreducible error floor. On safety alignment, our method achieves up to 99.6% safety rate—exceeding full fine-tuning by 7.4 percentage points and approaching RLHF-based methods—while updating only 0.19–0.24% of parameters. Crucially, our method provides interpretable insights into the learned alignment subspace through the semantic grounding of SAE features. Our work demonstrates that incorporating mechanistic interpretability into the fine-tuning process can simultaneously improve both performance and transparency.

## 1 Introduction

Large language models (LLMs) have achieved remarkable performance across diverse natural language processing tasks, owing to their strong generalization capabilities acquired through large-scale pre-training (Touvron et al., 2023; Achiam et al., 2023; Team et al., 2023). However, adapting these models to specific downstream tasks or aligning them with desired behaviors remains challenging.

Full fine-tuning, while effective, requires updating all model parameters, incurring prohibitive computational and memory costs that scale with model size (Liu et al., 2024).

Parameter-efficient fine-tuning (PEFT) methods have emerged as a practical solution, enabling model adaptation through a small subset of trainable parameters (Houlsby et al., 2019; Lester et al., 2021). Among these, Low-Rank Adaptation (LoRA) (Hu et al., 2021) has become particularly popular due to its simplicity and effectiveness. LoRA parameterizes weight updates as a low-rank decomposition  $\Delta\mathbf{W} = \mathbf{B}\mathbf{A}$ , resting on the hypothesis that task-relevant updates occupy a low-rank subspace (Aghajanyan et al., 2020; Li et al., 2018). This approach has been successfully applied across diverse domains, including instruction tuning (Zhang et al., 2023b), domain adaptation (Cheng et al., 2023), and notably, safety alignment (Hsu et al., 2024; Qi et al., 2024a).

Safety alignment is critical for responsible LLM deployment, as models must recognize and refuse harmful requests while maintaining helpfulness on benign inputs (Bai et al., 2022; Ouyang et al., 2022). Recent work has demonstrated that LoRA can effectively align models for safety with minimal computational overhead (Xue et al., 2025), and that safety-related behaviors may be governed by low-rank structures in model weights (Arditi et al., 2024; Wei et al., 2024). These findings suggest that principled identification of safety-relevant subspaces could enhance both the efficiency and reliability of alignment.

However, existing low-rank adaptation methods face two fundamental limitations. First, the learned subspace remains opaque: optimization discovers task-relevant directions implicitly, providing no insight into which semantic concepts the adapter modulates. Second, recent work reveals a fundamental asymmetry in LoRA: the  $\mathbf{B}$  matrix, which projects to the output space, plays the dominant

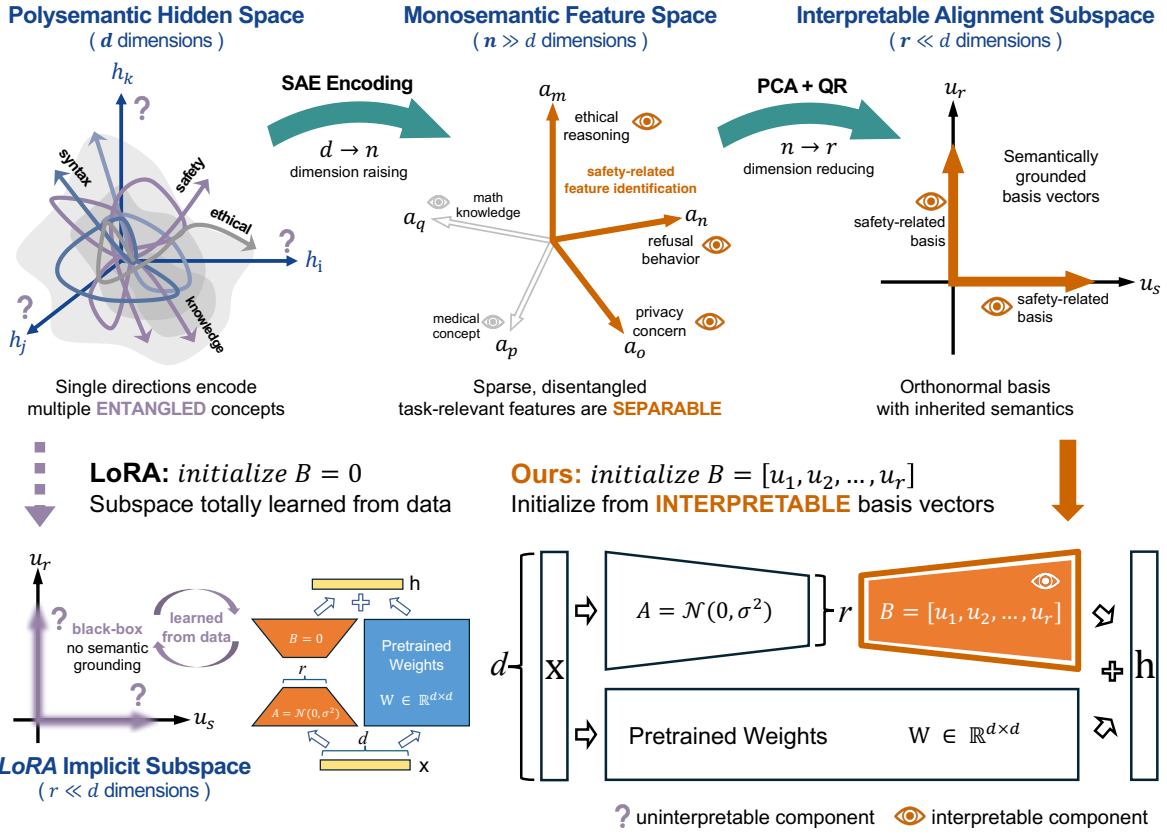


Figure 1: Overview of our method. **Top:** SAEs transform polysemantic hidden states into a disentangled feature space where task-relevant directions become separable, enabling construction of an interpretable alignment subspace via PCA and QR decomposition. **Bottom:** Unlike LoRA which learns subspaces implicitly from data, we initialize  $B$  with semantically grounded basis vectors derived from SAE decoder directions.

role in adaptation, while  $A$  primarily serves as a feature extractor (Zhu et al., 2024). This implies that the choice of output subspace is critical—yet this subspace is learned implicitly rather than constructed principally. We hypothesize that an underexplored contributing factor is the *difficulty of identifying appropriate subspaces* in the presence of polysemantic representations.

The challenge stems from a fundamental property of neural network representations: *polysemy* (Olah et al., 2020). According to the superposition hypothesis (Elhage et al., 2022), LLMs encode more semantic features than they have dimensions, resulting in individual neurons responding to multiple unrelated concepts. This *semantic entanglement* makes it difficult to isolate subspaces associated with specific tasks or behaviors directly in the model’s hidden space. As Zhang (2025) observe: “this semantic entanglement makes it difficult to isolate subspaces specifically associated with [task-relevant] content.”

Recent advances in mechanistic interpretability

offer a potential solution. Sparse Autoencoders (SAEs) learn to decompose polysemantic activations into a higher-dimensional, sparse feature space where individual dimensions correspond to monosemantic concepts (Cunningham et al., 2023; Bricken et al., 2023; Templeton et al., 2024). SAE features have been successfully used for activation steering (O’Brien et al., 2024; Turner et al., 2023) and understanding safety-related behaviors (Arditi et al., 2024; Yeo et al., 2025). Critically, each SAE feature is associated with a decoder direction that represents an interpretable semantic concept in the original representation space.

In this work, we propose a method for interpretable safety alignment via SAE-constructed low-rank subspace adaptation, bridging mechanistic interpretability and parameter-efficient fine-tuning. Our key insight is that the difficulty of subspace identification can be resolved by operating in the disentangled SAE feature space, where task-relevant directions become readily separable. Specifically, we (1) identify features whose acti-

vations differ between aligned and unaligned behaviors, (2) extract the corresponding SAE decoder directions to construct an interpretable low-rank subspace, and (3) use this subspace to initialize the LoRA adapter’s output projection matrix. Drawing on recent findings that the  $\mathbf{B}$  matrix plays the dominant role in LoRA adaptation (Zhu et al., 2024), our initialization provides a principled, interpretable starting point for optimization.

Our contributions can be summarized as follows:

- We propose a novel SAE-based feature analysis method and empirically demonstrate its effectiveness in identifying interpretable features with significant impact on model safety performance.
- We introduce a method for SAE-constructed low-rank subspace adaptation that builds an explicit, interpretable task-relevant subspace from SAE decoder directions. Experiments across multiple model scales and families show that our approach achieves safety alignment performance substantially exceeding full fine-tuning and approaching reinforcement learning-based methods, while updating only 0.19–0.24% of parameters.
- We provide rigorous theoretical analysis showing that SAE-based subspace identification achieves arbitrarily small recovery error under monosemanticity assumptions, whereas direct identification in the original polysemantic space suffers an irreducible error floor of  $\sqrt{r-1}$  for  $r$ -dimensional subspaces.

## 2 Related Work

### 2.1 Parameter-Efficient Fine-Tuning

Parameter-efficient fine-tuning (PEFT) methods reduce the computational burden of adapting large pre-trained models by updating only a small subset of parameters. Existing approaches fall into three main categories.

**Adapter-based Methods.** These approaches introduce additional trainable modules into the frozen backbone. Houlsby et al. (2019) proposed sequential adapter layers, while He et al. (2022) demonstrated that parallel adapters can improve performance. Subsequent work has explored various architectural designs (Mahabadi et al., 2021; Pfeiffer et al., 2021) and efficient adapter combinations (Pfeiffer et al., 2021).

**Prompt-based Methods.** Prompt tuning (Lester et al., 2021) and prefix tuning (Li and Liang, 2021) prepend learnable soft tokens to the input, training only these continuous vectors. While effective, these methods often exhibit sensitivity to initialization and can increase inference latency due to extended sequence lengths (Razdaibiedina et al., 2023; Wang et al., 2023).

**Low-Rank Adaptation.** LoRA (Hu et al., 2021) and its variants represent weight updates as low-rank matrices, introducing no inference overhead since updates can be merged with pre-trained weights. Numerous extensions have been proposed: AdaLoRA (Zhang et al., 2023a) adaptively allocates ranks across layers; DoRA (Liu et al., 2024) decomposes updates into magnitude and direction components; VeRA (Kopczko et al., 2024) shares frozen random matrices across layers with learnable scaling vectors; and FourierFT (Gao et al., 2024) operates in the frequency domain. Despite these advances, the learned subspaces remain opaque, and the fundamental question of *which* subspace to adapt is typically left to implicit optimization. Our work addresses this gap by explicitly constructing an interpretable subspace prior to training.

Critically, Zhu et al. (2024) revealed a fundamental asymmetry: the  $\mathbf{B}$  matrix plays the dominant role in LoRA adaptation, defining the output subspace, while  $\mathbf{A}$  can be fixed at random initialization. This finding motivates our approach of explicitly constructing  $\mathbf{B}$  from interpretable directions.

### 2.2 Safety Alignment of LLMs

Ensuring that LLMs refuse harmful requests while remaining helpful is a central challenge in AI safety (Bai et al., 2022; Ouyang et al., 2022). Traditional approaches include reinforcement learning from human feedback (RLHF) (Christiano et al., 2017; Ziegler et al., 2019) and direct preference optimization (DPO) (Rafailov et al., 2023), which optimize models against human preferences but require substantial computational resources and careful reward modeling.

Recent work has explored more efficient alignment approaches. Xue et al. (2025) demonstrate that LoRA-based supervised fine-tuning can achieve safety alignment comparable to full fine-tuning while preserving reasoning capabilities. Safe LoRA (Hsu et al., 2024) projects LoRA updates onto a safety-aligned subspace derived from

the difference between base and aligned model weights, mitigating safety degradation during fine-tuning. SPLoRA (Cao, 2025) prunes LoRA layers that deviate from safety alignment. These methods operate on weight differences between model versions, whereas our approach constructs subspaces directly from interpretable SAE features, providing semantic grounding for the alignment process.

### 2.3 Representation Engineering and Activation Steering

Representation engineering (Zou et al., 2023a) provides a framework for understanding and controlling LLM behavior by identifying directions in activation space associated with high-level concepts. Building on the linear representation hypothesis (Park et al., 2024; Mikolov et al., 2013), this approach has been applied to steer behaviors including truthfulness (Marks and Tegmark, 2023), refusal (Arditi et al., 2024), and fairness (Adila et al., 2024).

Contrastive Activation Addition (CAA) (Rimsky et al., 2024) constructs steering vectors by averaging activation differences between positive and negative examples. Conditional Activation Steering (CAST) (Lee et al., 2024) enables selective refusal by conditioning on prompt patterns. However, activation steering at inference time can degrade model performance (O’Brien et al., 2024; Pres et al., 2024), as the steering vectors may interfere with other model capabilities due to entangled representations. Our method sidesteps this issue by integrating interpretable directions into the fine-tuning process rather than applying them at inference time.

### 2.4 Sparse Autoencoders for Interpretability

Sparse Autoencoders (SAEs) have emerged as a powerful tool for mechanistic interpretability, learning to decompose model activations into sparse, monosemantic features (Cunningham et al., 2023; Bricken et al., 2023). Unlike the polysemantic neurons in the original model, SAE features tend to correspond to interpretable concepts, enabling precise analysis and manipulation of model behavior.

Templeton et al. (2024) demonstrated that SAEs scale to frontier models, extracting millions of interpretable features from Claude 3 Sonnet. Kissane et al. (2024) applied SAEs to attention layer outputs, revealing causally meaningful intermediate variables. Recent work has leveraged SAE features for model steering: O’Brien et al. (2024) identified

features mediating refusal behavior in Phi-3 Mini; Yeo et al. (2025) conducted mechanistic studies of refusal using SAE-derived features; and SRS (Liu, 2025) proposed sparse representation steering for fine-grained control over safety, fairness, and truthfulness.

Most closely related to our work, Zhang (2025) used SAEs to identify and intervene on copyright-sensitive subspaces, explicitly noting that polysemy makes direct subspace isolation difficult. However, their approach focuses on inference-time interventions rather than adapter training. We extend this insight by using SAE decoder directions to construct low-rank subspaces for LoRA initialization, bridging mechanistic interpretability and parameter-efficient fine-tuning.

### 2.5 Intrinsic Dimensionality and LoRA Asymmetry

The effectiveness of low-rank adaptation rests on the hypothesis that task-relevant updates occupy a low-dimensional subspace (Li et al. (2018); Aghajanyan et al. (2020)). Our work builds on this foundation by constructing such subspaces explicitly from interpretable features rather than learning them implicitly.

## 3 Semantic Disentanglement Enables Tractable Low-Rank Subspace Identification

Before presenting our method, we establish a theoretical foundation for why task-relevant low-rank subspaces are fundamentally easier to identify in the sparse semantic space revealed by SAEs than in the original polysemantic representation space. We formalize this as a *subspace recovery problem* and prove that SAE-based identification achieves arbitrarily small recovery error, whereas direct identification in the original space suffers an irreducible error floor.

### 3.1 Problem Formulation

We adopt a semantic generative model where hidden representations arise from sparse combinations of underlying semantic concepts.

**Definition 1** (Semantic Generative Model). *Let  $\mathbf{s} = (s_1, \dots, s_N)^\top \in \mathbb{R}_{\geq 0}^N$  be the activation vector over  $N$  semantic concepts. The original representation  $\mathbf{h} \in \mathbb{R}^d$  is generated as:*

$$\mathbf{h} = W\mathbf{s} + \xi, \quad W \in \mathbb{R}^{d \times N}, \quad d < N \quad (1)$$

where  $W$  encodes the  $N$  semantic directions via superposition (Elhage et al., 2022), and  $\xi$  is noise. The SAE encoder  $\phi : \mathbb{R}^d \rightarrow \mathbb{R}^n$  with  $n \geq N$  produces activations  $\mathbf{a} = \phi(\mathbf{h}) = D\mathbf{s} + \mathbf{e}$ , where  $D \in \mathbb{R}^{n \times N}$  and  $\mathbf{e}$  is bounded reconstruction error.

For safety alignment, we consider two classes of inputs: aligned (e.g., safe refusals) and unaligned (e.g., harmful completions). A subset  $\mathcal{T} \subseteq \{1, \dots, N\}$  of  $r$  features are *task-relevant*—their activations differ systematically between classes.

**Definition 2** (Task-Relevant Subspace). *Let  $\mathcal{T}$  with  $|\mathcal{T}| = r \geq 2$  index the task-relevant features. The task-relevant subspace is  $\mathcal{S} = \text{span}(\{\mathbf{w}_i\}_{i \in \mathcal{T}})$  where  $\mathbf{w}_i = W_{:,i}$  denotes the  $i$ -th semantic direction.*

**Definition 3** (Subspace Recovery Error). *For subspaces  $\mathcal{U}, \mathcal{V}$ , the recovery error is  $E(\mathcal{U}, \mathcal{V}) = \|P_{\mathcal{U}} - P_{\mathcal{V}}\|_F$ , where  $P_{\mathcal{U}}, P_{\mathcal{V}}$  are orthogonal projections onto the respective subspaces.*

### 3.2 Recovery Procedures and Assumptions

We compare two recovery procedures. The **original space method** computes the mean difference  $\delta_h = \bar{\mathbf{h}}^{(1)} - \bar{\mathbf{h}}^{(2)}$  between class-conditional means and returns  $\hat{\mathcal{S}}_{\text{orig}} = \text{span}(\delta_h)$ . The **SAE space method** computes  $\delta_a = \bar{\mathbf{a}}^{(1)} - \bar{\mathbf{a}}^{(2)}$ , selects features  $\hat{\mathcal{T}} = \{i : |[\delta_a]_{k_i}| > \tau\}$  exceeding a threshold, and returns  $\hat{\mathcal{S}}_{\text{SAE}} = \text{span}(\{W_{\text{dec}}[:, k_i]\}_{i \in \hat{\mathcal{T}}})$ .

Our analysis relies on two key assumptions capturing the monosemanticity property of well-trained SAEs:

**Assumption 1** (Task-Semantic Separation). *Task-relevant features exhibit class separation:  $|\mu_i^{(1)} - \mu_i^{(2)}| \geq \delta > 0$  for  $i \in \mathcal{T}$ , while non-task features show no separation:  $|\mu_j^{(1)} - \mu_j^{(2)}| = 0$  for  $j \notin \mathcal{T}$ .*

**Assumption 2** (SAE Monosemanticity). *There exists a feature correspondence  $\kappa$  such that: (a) each semantic concept  $i$  activates a dedicated SAE feature  $k_i$  with strength  $d_i \geq d_{\min} > 0$ ; (b) cross-talk between features is bounded by  $\epsilon^2/r$ ; and (c) the SAE decoder directions  $W_{\text{dec}}[:, k_i]$  approximate the true semantic directions with error bounded by  $\nu$ .*

### 3.3 Main Theoretical Results

Our main results establish a fundamental asymmetry between the two recovery procedures.

**Theorem 4** (Original Space Recovery Error). *Under Assumptions 1–2, the original space method has recovery error:*

$$E(\hat{\mathcal{S}}_{\text{orig}}, \mathcal{S}) = \sqrt{r-1} \quad (2)$$

*This error is exact and irreducible regardless of sample size.*

The intuition is that the mean difference  $\delta_h = \sum_{i \in \mathcal{T}} \mathbf{w}_i \Delta_i$  is a single vector lying within the  $r$ -dimensional subspace  $\mathcal{S}$ . Thus,  $\hat{\mathcal{S}}_{\text{orig}}$  recovers only a one-dimensional projection, leaving the remaining  $r-1$  dimensions unrecovered.

**Theorem 5** (SAE Space Recovery Error). *Under Assumptions 1–2, if monosemanticity is sufficiently strong (bounded cross-talk and small decoder alignment error  $\nu$ ), then the SAE method achieves:*

$$E(\hat{\mathcal{S}}_{\text{SAE}}, \mathcal{S}) \leq \frac{2\sqrt{r}\nu}{\sigma_0 - \sqrt{r}\nu} \quad (3)$$

*where  $\sigma_0$  is the minimum singular value of the task-relevant direction matrix.*

Critically, this bound can be made arbitrarily small by improving SAE quality (reducing  $\nu$ ), whereas the original space error  $\sqrt{r-1}$  is intrinsic to the method.

**Theorem 6** (Recovery Error Comparison). *For any target error  $\varepsilon \in (0, \sqrt{r-1})$ , if the SAE decoder alignment satisfies  $\nu < \frac{\varepsilon\sigma_0}{\sqrt{r}(2+\varepsilon)}$ , then  $E(\hat{\mathcal{S}}_{\text{SAE}}, \mathcal{S}) < \varepsilon$  while  $E(\hat{\mathcal{S}}_{\text{orig}}, \mathcal{S}) = \sqrt{r-1}$ .*

Full proofs are provided in Appendix A. The key insight is that SAE monosemanticity transforms the subspace recovery problem into a feature selection problem: rather than recovering directions from a superimposed signal, we identify which individual features are task-relevant and retrieve their known decoder directions.

### 3.4 Implications for Low-Rank Adapter Design

The LoRA asymmetry phenomenon (Zhu et al., 2024) reveals that the  $\mathbf{B}$  matrix plays the dominant role in adaptation, defining the *output subspace* that the adapter can influence. Our theoretical results motivate explicitly constructing  $\mathbf{B}$  using SAE-derived directions:

$$\mathbf{B}^{(0)} = \alpha \cdot \mathbf{U}_{\text{task}}[:, 1:r] \quad (4)$$

where  $\mathbf{U}_{\text{task}}$  is an orthonormal basis for the identified subspace.

This initialization offers three advantages: (1) an informed starting point within the provably identifiable task-relevant subspace, (2) interpretability through correspondence to SAE decoder directions, and (3) theoretical grounding from the recovery error bounds established above.

## 4 Methodology

Our theoretical analysis (Section 3) establishes that SAE-based subspace identification achieves arbitrarily small recovery error, while direct identification in polysemantic space suffers an irreducible error floor. We now present our practical algorithm that operationalizes these insights.

### 4.1 SAE-Based Feature Identification

The first step identifies task-relevant features in the SAE’s interpretable feature space. Given a pre-trained SAE with encoder  $f_{\text{enc}} : \mathbb{R}^d \rightarrow \mathbb{R}^n$  and decoder  $f_{\text{dec}} : \mathbb{R}^n \rightarrow \mathbb{R}^d$ , where  $d$  is the model’s hidden dimension and  $n \gg d$  is the SAE feature dimension, we collect activations on two contrasting datasets: an aligned dataset  $\mathcal{D}_{\text{aligned}}$  (e.g., safe responses) and an unaligned dataset  $\mathcal{D}_{\text{unaligned}}$  (e.g., unsafe responses).

For each input  $x$ , we extract the hidden state  $\mathbf{h}_\ell^{(x)} \in \mathbb{R}^d$  at layer  $\ell$  and compute the SAE feature activations:

$$\mathbf{a}_\ell^{(x)} = f_{\text{enc}}(\mathbf{h}_\ell^{(x)}) \in \mathbb{R}^n \quad (5)$$

For each feature  $i$  at layer  $\ell$ , we compute the mean activation difference between the two distributions:

$$\Delta_{\ell,i} = \left| \mathbb{E}_{x \sim \mathcal{D}_{\text{aligned}}} [a_{\ell,i}^{(x)}] - \mathbb{E}_{x \sim \mathcal{D}_{\text{unaligned}}} [a_{\ell,i}^{(x)}] \right| \quad (6)$$

We then compute the relative activation difference to identify features whose activation patterns differ most substantially between aligned and unaligned behaviors:

$$\rho_{\ell,i} = \frac{\Delta_{\ell,i}}{\max \left( \mathbb{E}_{x \sim \mathcal{D}_{\text{unaligned}}} [|a_{\ell,i}^{(x)}|], \epsilon \right)} \times 100 \quad (7)$$

where  $\epsilon$  is a small constant for numerical stability. Features with high  $\rho_{\ell,i}$  values indicate semantic directions that are differentially activated based on alignment status, making them candidates for constructing the task-relevant subspace.

For each layer  $\ell$ , we select the top- $k$  features based on their activation differences, yielding the safety-relevant feature set  $\mathcal{F}_\ell = \{i : \Delta_{\ell,i} \in \text{top-}k\}$ . This selection ensures that the subsequent subspace construction captures the most discriminative semantic directions for the target task.

### 4.2 Subspace Construction via Decoder Directions

The second step constructs an interpretable low-rank subspace using the decoder directions of identified features. For a pre-trained SAE, each feature  $i$  corresponds to a decoder direction  $\mathbf{d}_i \in \mathbb{R}^d$  that represents a semantically meaningful direction in the model’s representation space (Cunningham et al., 2023). The decoder weight matrix  $\mathbf{W}_{\text{dec}} \in \mathbb{R}^{n \times d}$  encodes these directions as its rows.

Given the identified feature set  $\mathcal{F}_\ell$  for layer  $\ell$ , we extract the corresponding decoder directions and form a direction matrix:

$$\mathbf{D}_\ell = [\mathbf{d}_{i_1}, \mathbf{d}_{i_2}, \dots, \mathbf{d}_{i_m}]^\top \in \mathbb{R}^{m \times d} \quad (8)$$

where  $m = |\mathcal{F}_\ell|$  is the number of selected features and  $\{i_1, \dots, i_m\}$  are the feature indices.

**Dimensionality Reduction via PCA.** The direction matrix  $\mathbf{D}_\ell$  may contain redundant or correlated directions. We apply Principal Component Analysis (PCA) to extract the principal components that capture the majority of variance in the identified directions. Specifically, we perform eigendecomposition on the covariance matrix:

$$\mathbf{C}_\ell = \mathbf{D}_\ell^\top \mathbf{D}_\ell \quad (9)$$

and select the top- $r$  eigenvectors  $\{\mathbf{v}_1, \dots, \mathbf{v}_r\}$  that collectively explain at least  $\tau$  proportion of the total variance (e.g.,  $\tau = 0.8$ ). This yields a principal component matrix:

$$\mathbf{V}_\ell = [\mathbf{v}_1, \mathbf{v}_2, \dots, \mathbf{v}_r]^\top \in \mathbb{R}^{r \times d} \quad (10)$$

**Orthogonal Subspace Decomposition.** To obtain a set of orthonormal basis vectors that span the task-relevant subspace, we perform QR decomposition on the transpose of the principal component matrix:

$$\mathbf{V}_\ell^\top = \mathbf{Q}_\ell \mathbf{R}_\ell \quad (11)$$

where  $\mathbf{Q}_\ell \in \mathbb{R}^{d \times d}$  is an orthogonal matrix obtained via complete QR factorization. We partition the columns of  $\mathbf{Q}_\ell$  into two orthogonal subspaces:

$$\begin{aligned} \mathbf{U}_{\text{align}}^{(\ell)} &= \mathbf{Q}_\ell[:, :r] \in \mathbb{R}^{d \times r}, \\ \mathbf{U}_{\text{orth}}^{(\ell)} &= \mathbf{Q}_\ell[:, r:] \in \mathbb{R}^{d \times (d-r)} \end{aligned} \quad (12)$$

where  $\mathbf{U}_{\text{align}}^{(\ell)}$  spans the alignment-relevant subspace and  $\mathbf{U}_{\text{orth}}^{(\ell)}$  spans its orthogonal complement. This decomposition enables us to project any vector onto the task-relevant subspace or its complement.

The corresponding projection matrices are:

$$\begin{aligned}\mathbf{P}_{\text{align}}^{(\ell)} &= \mathbf{U}_{\text{align}}^{(\ell)} (\mathbf{U}_{\text{align}}^{(\ell)})^\top, \\ \mathbf{P}_{\text{orth}}^{(\ell)} &= \mathbf{U}_{\text{orth}}^{(\ell)} (\mathbf{U}_{\text{orth}}^{(\ell)})^\top\end{aligned}\quad (13)$$

### 4.3 Subspace-Guided Adapter Training

The final step leverages the constructed subspace to guide LoRA adapter initialization and training.

**Subspace-Guided Initialization.** Following LoRA (Hu et al., 2021), we parameterize the weight update as  $\Delta \mathbf{W} = \mathbf{B} \mathbf{A}$ , where  $\mathbf{A} \in \mathbb{R}^{r \times d_{\text{in}}}$  and  $\mathbf{B} \in \mathbb{R}^{d_{\text{out}} \times r}$ . We set the LoRA rank  $r$  equal to the dimensionality of the identified safety-relevant subspace from Section 4.2, establishing a direct correspondence between the theoretical subspace dimension and the adapter capacity. Standard LoRA initializes  $\mathbf{A}$  with random Kaiming initialization and  $\mathbf{B}$  with zeros to ensure the initial weight update is zero.

We propose to initialize  $\mathbf{B}$  using the alignment subspace basis instead:

$$\mathbf{B} \leftarrow \alpha \cdot [\mathbf{u}_1, \mathbf{u}_2, \dots, \mathbf{u}_r] \quad (14)$$

where  $\{\mathbf{u}_1, \dots, \mathbf{u}_r\}$  are the columns of  $\mathbf{U}_{\text{align}}^{(\ell)}$  and  $\alpha$  is a scaling factor controlling the initialization magnitude. When the subspace dimension exceeds the LoRA rank ( $r' > r$ ), we use the first  $r$  basis vectors; when it is smaller ( $r' < r$ ), we zero-pad the remaining columns.

This initialization strategy offers two key advantages: (1) it provides a strong inductive bias by starting optimization within the identified task-relevant subspace, and (2) it inherits the interpretability of the SAE features, as each column of  $\mathbf{B}$  corresponds to a semantically meaningful direction.

**Optional Subspace Constraint Loss.** To further encourage the adapter to operate within the alignment-relevant subspace during training, we optionally introduce a subspace constraint loss. Given the hidden state  $\mathbf{h}_\ell$  at layer  $\ell$ , we penalize activations that fall outside the alignment subspace:

$$\mathcal{L}_{\text{sub}} = \frac{1}{|\mathcal{T}|} \sum_{\ell \in \mathcal{T}} \left\| \mathbf{P}_{\text{orth}}^{(\ell)} \mathbf{h}_\ell \right\|_2^2 \quad (15)$$

where  $\mathcal{T}$  denotes the set of target layers. This loss encourages the model’s representations to align with the identified task-relevant directions.

---

### Algorithm 1 Subspace-Guided Alignment via SAE

---

**Require:** Pre-trained LLM  $\mathcal{M}$ , SAE  $f$ , aligned data  $\mathcal{D}_{\text{aligned}}$ , unaligned data  $\mathcal{D}_{\text{unaligned}}$ , training data  $\mathcal{D}_{\text{train}}$ , target layers  $\mathcal{T}$ , variance threshold  $\tau$ , scaling factor  $\alpha$ , constraint weight  $\lambda$

**Ensure:** Fine-tuned model with LoRA adapters

- 1: // Stage 1: Feature Identification
- 2: for each layer  $\ell \in \mathcal{T}$  do
- 3:   Collect SAE activations on  $\mathcal{D}_{\text{aligned}}$  and  $\mathcal{D}_{\text{unaligned}}$
- 4:   Compute change magnitudes  $\Delta_{\ell,i}$  for all features  $i$
- 5:   Select top- $k$  features:  $\mathcal{F}_\ell \leftarrow \text{TopK}(\{\Delta_{\ell,i}\}_i)$
- 6: end for
- 7: // Stage 2: Subspace Construction
- 8: for each layer  $\ell \in \mathcal{T}$  do
- 9:   Extract decoder directions:  $\mathbf{D}_\ell \leftarrow [\mathbf{d}_i]_{i \in \mathcal{F}_\ell}$
- 10:   Apply PCA:  $\mathbf{V}_\ell \leftarrow \text{PCA}(\mathbf{D}_\ell, \tau)$
- 11:   QR decomposition:  $\mathbf{U}_{\text{align}}^{(\ell)}, \mathbf{U}_{\text{orth}}^{(\ell)} \leftarrow \text{QR}(\mathbf{V}_\ell^\top)$
- 12: end for
- 13: // Stage 3: Adapter Training
- 14: Initialize LoRA adapters with  $\mathbf{B} \leftarrow \alpha \cdot \mathbf{U}_{\text{align}}^{(\ell)}[:, :r]$
- 15: for each epoch do
- 16:   for each batch in  $\mathcal{D}_{\text{train}}$  do
- 17:     Compute  $\mathcal{L}_{\text{LM}}$  (language modeling loss)
- 18:     Compute  $\mathcal{L}_{\text{sub}}$  (subspace constraint loss)
- 19:     Update parameters via  $\nabla(\mathcal{L}_{\text{LM}} + \lambda \mathcal{L}_{\text{sub}})$
- 20:   end for
- 21: end for
- 22: return Fine-tuned model

---

The total training objective combines the standard language modeling loss with the optional subspace constraint:

$$\mathcal{L} = \mathcal{L}_{\text{LM}} + \lambda \mathcal{L}_{\text{sub}} \quad (16)$$

where  $\lambda$  is a hyperparameter controlling the strength of the subspace constraint.

### 4.4 Algorithm Summary

Algorithm 1 summarizes the complete procedure. The method can operate in two modes: (1) initialization-only mode, which uses subspace-guided initialization without the constraint loss, and (2) full mode, which combines both initialization and constraint loss.

## 4.5 Efficiency Analysis

Our method introduces minimal computational overhead during training while significantly reducing the number of trainable parameters required for effective alignment.

**Parameter Efficiency.** The trainable parameters consist solely of the LoRA matrices  $\mathbf{A}$  and  $\mathbf{B}$  for each target layer. For a model with hidden dimension  $d$  and LoRA rank  $r$ , the number of trainable parameters per layer is  $2rd$ . Our method achieves strong alignment performance with  $r = 16$ , corresponding to approximately 0.02% of the total model parameters.

**Memory Footprint.** The subspace construction is performed once before training and incurs negligible memory overhead. During training, the additional memory cost arises from: (1) storing the projection matrices  $\mathbf{P}_{\text{orth}}^{(\ell)}$  for each target layer, requiring  $d^2$  elements per layer, and (2) computing the subspace constraint loss, which involves matrix-vector products. The activation memory for our method is:

$$\mathcal{M}_{\text{ours}} = B \cdot S \cdot H + B \cdot r + |\mathcal{T}| \cdot d^2 \quad (17)$$

where  $B$  is the batch size,  $S$  is the sequence length,  $H$  is the hidden dimension, and  $|\mathcal{T}|$  is the number of target layers. The last term ( $|\mathcal{T}| \cdot d^2$ ) represents the pre-computed projection matrices, which are stored as constants and do not participate in gradient computation.

**Interpretability Benefit.** Unlike standard LoRA approaches where the learned subspace remains opaque, our method provides built-in interpretability. Each basis vector in  $\mathbf{U}_{\text{align}}^{(\ell)}$  corresponds to a linear combination of SAE decoder directions, which themselves encode interpretable semantic concepts. This enables post-hoc analysis of which safety-relevant features the adapter has learned to modulate.

## 5 Experiments

We conduct comprehensive experiments to evaluate our method on safety alignment tasks. We first describe the experimental setup, then present the main results comparing against baseline methods, followed by detailed ablation studies examining the effects of layer selection, SAE width, and interpretability analysis.

## 5.1 Baselines

We compare our method against the following baselines:

**Full Fine-Tuning (FFT)** updates all parameters of the model, representing the upper bound of adaptation capacity but with significant computational cost.

**LoRA** (Hu et al., 2021) approximates weight updates using low-rank matrices  $\Delta \mathbf{W} = \mathbf{B} \mathbf{A}$ , where  $\mathbf{A} \in \mathbb{R}^{r \times d}$  and  $\mathbf{B} \in \mathbb{R}^{d \times r}$  with  $r \ll d$ . We apply LoRA to the query, key, value, and output projection matrices with rank  $r = 16$ .

**DoRA** (Liu et al., 2024) decomposes pre-trained weights into magnitude and direction components, applying LoRA for directional updates while separately learning magnitude scaling factors.

**Prompt-based Defense** prepends a safety-oriented system prompt instructing the model to refuse harmful requests. This represents a training-free baseline that relies solely on in-context guidance.

**Instruction-Tuned + RLHF (IT+RL)** refers to the official instruction-tuned model variants that have undergone extensive supervised fine-tuning and reinforcement learning from human feedback (Ouyang et al., 2022). For Gemma models, we use Gemma-2-2B-IT and Gemma-2-9B-IT (Team et al., 2023). For the Llama family, we use Llama-3.1-8B-Instruct (Dubey et al., 2024), which was trained using supervised fine-tuning on instruction-response pairs followed by RLHF and direct preference optimization (DPO) to align the model with human preferences for helpfulness and safety. These instruction-tuned variants represent the performance ceiling achieved through substantially more compute-intensive alignment procedures.

## 5.2 Safety Alignment

**Models.** We evaluate our method on three model families: Gemma 2 2B, Gemma 2 9B (Team et al., 2023), and Llama 3.1 8B (Dubey et al., 2024). For Gemma models, we utilize the pre-trained Sparse Autoencoders from Gemma Scope (Lieberum et al., 2024), which provides JumpReLU SAEs trained on residual stream activations across all layers with widths of 16K and 65K features. For Llama 3.1 8B, we employ the publicly available SAEs from Llama Scope (He et al., 2024), specifically using

the Llama3\_1-8B-Base-LXR-8x variant trained on residual stream positions with an expansion factor of  $8\times$ .

**Datasets.** For training, we use the red-team-attempts subset of the HH-RLHF dataset (Ganguli et al., 2022), which contains adversarial conversations where human red-teamers attempted to elicit harmful responses. Following the dataset documentation, the `rating` field indicates the red team member’s assessment of how successful they were at breaking the AI assistant on a Likert scale, where higher values indicate more successful attacks. We filter conversations with `rating=0`, representing instances where the model successfully maintained safe behavior—these constitute high-quality safety alignment training data. From the 16,475 filtered examples, we extract the first user-assistant exchange and partition the data with ratios of 0.05/0.70/0.20/0.05 for development (used for identifying safety-relevant SAE features), training, testing, and validation, yielding 823, 11,532, 3,297, and 823 examples respectively. To preserve general capabilities, we incorporate capability-retention data sampled from the Alpaca dataset (Taori et al., 2023) at a ratio of 0.25:1 relative to safety alignment data.

For evaluation, we employ complementary benchmarks targeting three key aspects of safety alignment. The **HH-RLHF test set** consists of held-out examples from the same distribution as training, evaluating in-distribution alignment performance. The **HEX-PHI benchmark** (Qi et al., 2024b) provides 330 harmful instructions spanning 11 categories of prohibited use cases derived from Meta’s Llama 2 and OpenAI’s usage policies, serving as an out-of-distribution safety evaluation. Additionally, we evaluate robustness against adversarial attacks using **GCG** (Zou et al., 2023b), a state-of-the-art white-box jailbreak method that optimizes adversarial suffixes to elicit harmful responses.

**Implementation Details.** Following the experimental protocol established by Hu et al. (2021), we describe our hyperparameter selection methodology. For all LoRA-based methods (LoRA, DoRA, and ours), we set rank  $r = 16$ ,  $\alpha = 32$ , and dropout = 0.1.

*Learning Rate Selection.* We tune learning rates on the development set for each method. Full fine-tuning achieves optimal performance with a learning rate of  $1 \times 10^{-5}$ , while LoRA, DoRA, and our

method perform best with  $5 \times 10^{-5}$ . This difference aligns with prior findings that low-rank methods benefit from larger learning rates due to their constrained parameter space.

*Rank Selection.* Following ablation experiments (Section 5.3), we select  $r = 16$  as it provides sufficient capacity for safety alignment while maintaining parameter efficiency.

*Layer Selection.* Guided by the layer selection analysis in Section 5.3.1, we target layers that exhibit strong separation between aligned and unaligned representations in the SAE feature space. For Gemma 2 2B (26 layers total), we uniformly sample from early-middle and middle-late regions, selecting layers 5, 10, 15, and 20. For Gemma 2 9B (42 layers) and Llama 3.1 8B (32 layers), we select layers 10, 15, 20, 25, and 30 to capture safety-relevant computations distributed across middle-to-late transformer blocks.

*Training Configuration.* We use the AdamW optimizer with weight decay 0.01 and gradient clipping at 1.0. Training employs early stopping with patience of 5 epochs based on validation safety rate. For subspace construction, we set the variance threshold  $\tau = 0.8$  and select the top 30% of features by activation difference magnitude. The initialization scaling factor  $\alpha$  is set to 0.1.

**Evaluation Metrics.** We evaluate safety using kimi-k2 as a judge following Qi et al. (2024b), which assigns harmfulness scores from 1 (safe refusal) to 5 (fully compliant with harmful request). We report the **Average Harmfulness Score** (lower is better), **Safety Rate** (percentage of responses with score  $\leq 2$ ), and **High-Risk Rate** (percentage of responses with score = 5). For adversarial robustness, we report the attack accuracy under GCG attacks (lower indicates better robustness).

For capability preservation, we evaluate on five standard benchmarks: ARC-Easy, ARC-Challenge (Clark et al., 2018), HellaSwag (Zellers et al., 2019), WinoGrande (Sakaguchi et al., 2021), and BoolQ (Clark et al., 2019). We report the average accuracy across these tasks. Note that instruction-tuned models (IT+RL) incorporate additional capability-enhancing data during their alignment phase; thus, direct capability comparison with base model fine-tuning methods is not appropriate, and we report their capability scores separately for reference.

**Results and Analysis.** Table 1 presents the main results on safety alignment. Our method consis-

tently achieves superior performance compared to baseline fine-tuning methods while using equivalent or fewer trainable parameters.

On Gemma 2 2B, Our Method achieves a harmfulness score of 1.17 with 96.8% safety rate and only 2.6% high-risk rate, substantially outperforming LoRA (1.56, 87.6%, 8.4%) and DoRA (1.54, 89.0%, 7.6%). Notably, our method matches the performance of the instruction-tuned model with RLHF (1.18, 94.6%, 2.6%), which requires orders of magnitude more compute for alignment. On the out-of-distribution HEx-PHI benchmark, Our Method achieves 1.08 compared to 1.46 for LoRA, demonstrating strong generalization. For adversarial robustness, our method reduces GCG attack success from 24.7 to 15.7, approaching the IT+RL baseline (15.1).

On Gemma 2 9B, our method demonstrates even stronger performance, achieving a harmfulness score of 1.02 with 99.6% safety rate and only 0.4% high-risk rate. This matches or *exceeds* the instruction-tuned baseline (1.08, 98.2%, 0.0%) on in-distribution safety metrics, suggesting that principled subspace identification can achieve competitive performance with RLHF while requiring substantially less compute.

On Llama 3.1 8B, Our Method achieves 1.03 harmfulness with 99.2% safety rate, substantially outperforming all baseline fine-tuning methods while approaching IT+RL performance. This cross-family result suggests that SAE-guided subspace construction can generalize across model architectures, though further evaluation on additional families is needed.

For capability preservation, Our Method maintains competitive performance on Gemma 2 2B (0.400 vs. 0.431 original), representing minimal degradation compared to full fine-tuning (0.321). On larger models, we observe a trade-off between safety and capability preservation, consistent with prior findings that stronger safety alignment can affect general capabilities (Bai et al., 2022). We note that IT+RL models show higher capability scores; however, these are not directly comparable as they incorporate additional capability-enhancing data during training.

### 5.3 Ablation Studies

We conduct extensive ablation studies on Gemma 2 2B to understand the contribution of each component and provide guidance for hyperparameter selection.

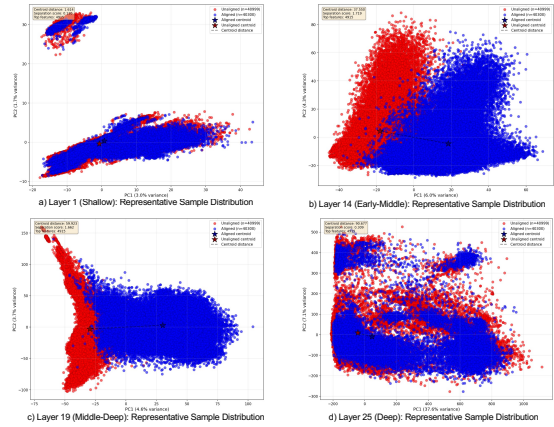


Figure 2: PCA visualization of SAE feature activations for aligned (blue) and unaligned (red) samples across different layers of Gemma 2 2B. Middle-deep layers (15–23) show the clearest separation, indicating concentrated encoding of safety-relevant concepts.

#### 5.3.1 Layer Selection Analysis

To determine the optimal target layers for subspace construction, we analyze how safety-relevant features are distributed across model layers. We first collect SAE activations on both aligned (safe refusals) and unaligned (harmful completions) examples, then visualize the feature space using PCA dimensionality reduction.

Figure 2 shows the PCA visualization of SAE feature activations at different layer depths. We observe distinct patterns across layer groups: shallow layers (0–6) show minimal separation between aligned and unaligned distributions; early-middle layers (7–14) begin to exhibit distributional divergence; middle-deep layers (15–23) achieve near-complete separation; and the deepest layers (24–25) show reduced discriminability. This pattern suggests that safety-relevant concepts are primarily encoded in middle-to-deep layers, consistent with findings that abstract semantic concepts emerge in later transformer layers (Elhage et al., 2022).

Based on this analysis, we evaluate different layer configurations in Table 2. Single-layer experiments confirm that middle-deep layers (15, 20) outperform shallow layers (5, 10). Combining layers from different depths yields further improvements, with the configuration using layers 5, 10, 15, and 20 achieving the best performance (1.17 harmfulness score, 96.8% safety rate). Interestingly, using all 26 layers degrades performance (1.38, 92.4%), suggesting that including irrelevant layers introduces noise into the subspace construction.

| Model        | Method      | # Params | HH-RLHF (Test)     |                 |                   | HEx-PHI $\downarrow$ | GCG $\downarrow$ | Cap. $\uparrow$ |
|--------------|-------------|----------|--------------------|-----------------|-------------------|----------------------|------------------|-----------------|
|              |             |          | Harm. $\downarrow$ | Safe $\uparrow$ | Risk $\downarrow$ |                      |                  |                 |
| Gemma-2-2B   | Original    | –        | 2.88               | 52.8%           | 42.4%             | 3.63                 | 32.6             | 0.431           |
|              | Prompt      | –        | 1.51               | 88.0%           | 8.8%              | 1.32                 | 21.3             | 0.392           |
|              | FFT         | 100%     | 1.52               | 89.2%           | 8.8%              | 1.39                 | 21.6             | 0.321           |
|              | LoRA        | 0.24%    | 1.56               | 87.6%           | 8.4%              | 1.46                 | 24.7             | 0.362           |
|              | DoRA        | 0.25%    | 1.54               | 89.0%           | 7.6%              | 1.31                 | 22.6             | 0.365           |
|              | <b>Ours</b> | 0.24%    | <b>1.17</b>        | <b>96.8%</b>    | <b>2.6%</b>       | <b>1.08</b>          | <b>15.7</b>      | <b>0.366</b>    |
| Gemma-2-9B   | IT+RL       | –        | 1.18               | 94.6%           | 2.6%              | 1.02                 | 15.1             | 0.495 $\dagger$ |
|              | Original    | –        | 2.73               | 57.6%           | 37.4%             | 3.95                 | 34.0             | 0.411           |
|              | Prompt      | –        | 1.29               | 94.2%           | 4.6%              | 1.26                 | 20.2             | 0.390           |
|              | FFT         | 100%     | 1.44               | 92.2%           | 7.0%              | 1.24                 | 19.7             | 0.313           |
|              | LoRA        | 0.19%    | 1.41               | 92.4%           | 4.8%              | 1.54                 | 20.3             | 0.350           |
|              | DoRA        | 0.20%    | 1.67               | 86.0%           | 10.2%             | 1.48                 | 20.3             | 0.340           |
| Llama-3.1-8B | <b>Ours</b> | 0.19%    | <b>1.02</b>        | <b>99.6%</b>    | <b>0.4%</b>       | <b>1.01</b>          | <b>13.1</b>      | <b>0.404</b>    |
|              | IT+RL       | –        | 1.08               | 98.2%           | 0.0%              | 1.00                 | 13.0             | 0.570 $\dagger$ |
|              | Original    | –        | 2.54               | 62.0%           | 35.2%             | 4.09                 | 31.1             | 0.674           |
|              | Prompt      | –        | 1.47               | 90.6%           | 7.6%              | 1.33                 | 21.6             | 0.545           |
|              | FFT         | 100%     | 1.34               | 92.8%           | 6.0%              | 1.16                 | 19.2             | 0.339           |
|              | LoRA        | 0.21%    | 1.40               | 92.0%           | 5.2%              | 1.27                 | 20.9             | 0.652           |
| Llama-3.1-8B | DoRA        | 0.22%    | 1.54               | 89.6%           | 7.6%              | 1.36                 | 22.0             | 0.670           |
|              | <b>Ours</b> | 0.21%    | <b>1.03</b>        | <b>99.2%</b>    | <b>0.8%</b>       | <b>1.03</b>          | <b>14.0</b>      | <b>0.670</b>    |
|              | IT+RL       | –        | 1.13               | 97.8%           | 2.6%              | 1.16                 | 14.7             | 0.685 $\dagger$ |

Table 1: Main results on safety alignment across three model families. We report harmfulness score (Harm. $\downarrow$ ), safety rate (Safe $\uparrow$ ), high-risk rate (Risk $\downarrow$ ), HEx-PHI harmfulness score, GCG attack accuracy (lower is better), and average capability preservation score (Cap.). Best results among fine-tuning methods are in **bold**. IT+RL represents instruction-tuned baselines trained with substantially more compute.  $\dagger$ Capability scores for IT+RL models are not directly comparable as they incorporate additional capability data during training.

| Target Layers            | Harm. $\downarrow$ | Safe $\uparrow$ | Risk $\downarrow$ |
|--------------------------|--------------------|-----------------|-------------------|
| Layer 5 (shallow)        | 1.27               | 95.4%           | 3.8%              |
| Layer 10 (early-mid)     | 1.32               | 92.8%           | 6.4%              |
| Layer 15 (mid-deep)      | 1.22               | 95.4%           | 4.0%              |
| Layer 20 (deep)          | 1.21               | 96.2%           | 3.2%              |
| Layers 5 + 15            | 1.31               | 93.6%           | 4.2%              |
| Layers 5 + 20            | 1.22               | 95.8%           | 3.8%              |
| Layers 10 + 15           | 1.22               | 95.6%           | 4.0%              |
| Layers 10 + 20           | 1.57               | 86.6%           | 12.8%             |
| <b>Layers 5+10+15+20</b> | <b>1.17</b>        | <b>96.8%</b>    | <b>2.6%</b>       |
| All layers (0–25)        | 1.38               | 92.4%           | 6.2%              |

Table 2: Layer selection ablation on Gemma 2 2B with 16K SAE width. Results show that combining layers across depths achieves optimal performance.

### 5.3.2 SAE Width Analysis

We investigate the effect of SAE width on alignment performance. Gemma Scope provides SAEs with widths of 16K and 65K features. Table 3 shows that 16K width achieves superior performance (1.17 vs. 1.25 harmfulness score). This suggests that wider SAEs may introduce feature splitting (Bricken et al., 2023), where semantic concepts become distributed across multiple correlated

| SAE Width  | Harm. $\downarrow$ | Safe $\uparrow$ | Risk $\downarrow$ |
|------------|--------------------|-----------------|-------------------|
| <b>16K</b> | <b>1.17</b>        | <b>96.8%</b>    | <b>2.6%</b>       |
| 65K        | 1.25               | 94.6%           | 5.4%              |

Table 3: SAE width ablation on Gemma 2 2B using layers 5, 10, 15, and 20.

features, potentially degrading the quality of the constructed subspace. The 16K width provides sufficient granularity for capturing safety-relevant concepts while avoiding excessive fragmentation.

### 5.3.3 Rank Selection Analysis

We investigate the effect of LoRA rank  $r$  on alignment performance. The rank determines the dimensionality of the constructed subspace and directly influences the adapter’s capacity to capture task-relevant directions. Table 4 presents results across ranks ranging from 1 to 32.

Performance improves substantially as rank increases from 1 to 16, with harmfulness score decreasing from 1.58 to 1.17 and safety rate increasing from 86.2% to 96.8%. Notably,  $r = 1$  corresponds to the theoretical limitation identified in Theorem 4: recovering only a single di-

| Rank ( $r$ ) | Harm. $\downarrow$ | Safe $\uparrow$ | Risk $\downarrow$ |
|--------------|--------------------|-----------------|-------------------|
| 1            | 1.58               | 86.2%           | 13.0%             |
| 2            | 1.43               | 91.4%           | 10.2%             |
| 4            | 1.27               | 91.5%           | 11.2%             |
| 8            | 1.21               | 92.2%           | 8.6%              |
| <b>16</b>    | <b>1.17</b>        | <b>96.8%</b>    | <b>2.6%</b>       |
| 32           | 1.17               | 96.8%           | 6.6%              |

Table 4: Rank selection ablation on Gemma 2 2B. Performance improves with increasing rank up to  $r = 16$ , beyond which additional capacity introduces noise directions.

rection yields suboptimal coverage of the multi-dimensional safety subspace. As rank increases, the adapter gains capacity to span more of the task-relevant subspace, leading to improved alignment.

However, increasing rank beyond 16 does not yield further improvements and may introduce degradation: while  $r = 32$  maintains the same harmfulness score (1.17), the high-risk rate increases from 2.6% to 6.6%. This suggests that excessively high ranks incorporate noise directions that lie outside the true safety-relevant subspace, consistent with the theoretical intuition that the task-relevant subspace has finite intrinsic dimensionality. Based on these results, we select  $r = 16$  for all main experiments as it achieves optimal performance while maintaining parameter efficiency.

### 5.3.4 Component Ablation

We ablate the two key components of our method: subspace-guided initialization and subspace constraint loss. Table 5 presents the results.

Using only subspace initialization (Init-only) achieves the best safety performance (1.17 harm score), demonstrating that providing the correct inductive bias at initialization is highly effective. Interestingly, the Loss-only configuration also shows positive effects compared to the LoRA baseline (1.42 vs. 1.56), indicating that the subspace constraint provides meaningful guidance even without principled initialization. However, combining both components (Init+Loss) results in slightly degraded safety (1.24 vs. 1.17) while maintaining better interpretability through stricter subspace preservation.

This trade-off reveals an important insight: the subspace constraint loss prevents the adapter from escaping the initial subspace to find potentially better solutions, but ensures the final model remains interpretable through the lens of the original SAE features. For our main experiments, we use the Init-only configuration to maximize safety perfor-

| Init | Loss | Harm. $\downarrow$ | Safe $\uparrow$ | Risk $\downarrow$ | Cap. $\uparrow$ |
|------|------|--------------------|-----------------|-------------------|-----------------|
| ✗    | ✗    | 1.56               | 87.6%           | 8.4%              | 0.362           |
| ✓    | ✗    | <b>1.17</b>        | <b>96.8%</b>    | <b>2.6%</b>       | <b>0.400</b>    |
| ✗    | ✓    | 1.42               | 90.4%           | 6.2%              | 0.358           |
| ✓    | ✓    | 1.24               | 95.2%           | 3.8%              | 0.395           |

Table 5: Component ablation on Gemma 2 2B. “Init” denotes subspace-guided initialization; “Loss” denotes subspace constraint loss. Init-only achieves best safety; Init+Loss trades safety for interpretability.

mance, while the Init+Loss variant is preferable when interpretability is the primary concern.

### 5.4 Interpretability Analysis

A key advantage of our method is the interpretability provided by grounding the alignment subspace in SAE features. We analyze the identified features to validate that our feature identification procedure successfully captures safety-relevant concepts.

**Feature Explanation Analysis.** For each identified feature, we obtain natural language explanations from Neuronpedia (Lin et al., 2024), which hosts auto-generated interpretations for Gemma Scope SAE features. We then use an LLM (Qwen-2.5-7B) to classify whether each explanation relates to safety concepts. Table 6 shows representative examples of identified safety-relevant features across different layers.

We find that our feature identification procedure selects a significantly higher proportion of safety-related features compared to random sampling. Across layers 5, 10, 15, and 20, approximately 35% of identified features relate to safety concepts (e.g., ethical reasoning, privacy protection, legal compliance), compared to less than 5% in random samples. This validates that our differential activation analysis successfully captures features relevant to the safety alignment task.

**Feature Intervention Experiments.** To further validate the causal relevance of identified features, we conduct intervention experiments following Templeton et al. (2024). We amplify or suppress the activations of identified safety features during inference and measure the effect on model outputs.

Figure 3 shows that amplifying safety-relevant features (scaling by  $1.5\times$ – $2\times$ ) reduces the toxicity of model outputs on harmful prompts, while suppressing these features (scaling by  $0.5\times$ – $0\times$ ) increases toxicity. This bidirectional effect con-

| Layer | Idx   | Explanation                                       | Category        |
|-------|-------|---|-----------------|
| 0     | 11049 | References to safety in medical contexts          | Medical Safety  |
| 1     | 6459  | Moral judgments and ethical considerations        | Moral Reasoning |
| 4     | 12428 | Personal and identifiable information             | Privacy         |
| 5     | 14087 | Statements about truthfulness or falsehood        | Misinformation  |
| 12    | 15454 | Governance and ethical considerations in research | Ethics          |
| 16    | 1377  | Data privacy and user consent                     | Privacy         |
| 18    | 15394 | Legal considerations and regulations              | Legal           |

Table 6: Examples of identified safety-relevant SAE features with their natural language explanations from Neuronpedia and associated safety categories.

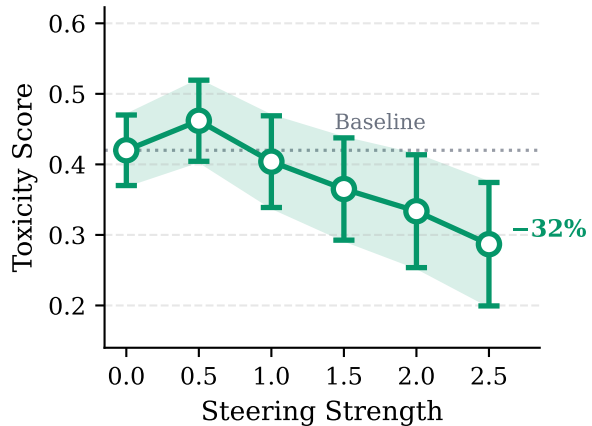


Figure 3: Feature intervention experiments. Amplifying identified safety features reduces output toxicity, while suppressing them increases toxicity, demonstrating causal relevance.

firms that the identified features causally influence safety-related behaviors, providing mechanistic validation of our feature identification approach.

### 5.5 Subspace Preservation Analysis

We analyze how the constructed alignment subspace evolves during fine-tuning by measuring the Grassmann distance between the initial LoRA B matrix (initialized with subspace basis vectors) and the final B matrix after training. The Grassmann distance quantifies the angle between subspaces, with smaller values indicating better preservation.

Table 7 compares subspace preservation between Init-only and Init+Loss configurations across all three model families. In the Init-only configuration, moderate subspace perturbation occurs dur-

| Model        | Config    | Grassmann $\downarrow$ | Angle $\downarrow$ |
|--------------|-----------|------------------------|--------------------|
| Gemma-2-2B   | Init-only | 3.27                   | 40.76°             |
|              | Init+Loss | 0.82                   | 10.19°             |
| Gemma-2-9B   | Init-only | 4.03                   | 53.67°             |
|              | Init+Loss | 1.01                   | 13.42°             |
| Llama-3.1-8B | Init-only | 3.52                   | 44.15°             |
|              | Init+Loss | 0.88                   | 11.04°             |

Table 7: Subspace preservation metrics comparing Init-only and Init+Loss configurations. Lower values indicate stricter preservation. Init-only allows beneficial refinement; Init+Loss enforces interpretability.

ing training (Grassmann distance 3.27–4.03, mean angle 40.76°–53.67°), indicating that the adapter refines within and beyond the initial subspace to discover improved alignment directions. In contrast, the Init+Loss configuration maintains strict subspace preservation (approximately 1/4 of Init-only values), as the constraint loss explicitly penalizes deviations from the original SAE-derived directions.

This analysis illuminates the trade-off observed in the component ablation: Init-only achieves superior safety performance by allowing beneficial subspace refinement, while Init+Loss preserves interpretability at the cost of constraining the optimization landscape. The moderate perturbation in Init-only suggests that while the SAE-derived subspace provides an excellent starting point, the optimization discovers nearby directions that further improve alignment. This finding supports our recommendation to use Init-only for maximum safety and Init+Loss when maintaining direct correspondence to SAE features is essential.

## 6 Conclusion

We proposed a method for interpretable safety alignment that leverages Sparse Autoencoders to construct explicit, semantically grounded subspaces for guiding low-rank adapter training. By identifying task-relevant features through differential activation analysis and using their decoder directions to initialize LoRA matrices, our approach provides a principled connection between mechanistic interpretability and parameter-efficient fine-tuning. Extensive experiments on safety alignment benchmarks demonstrate that our method not only outperforms existing PEFT methods in alignment effectiveness but also approaches the performance of compute-intensive RLHF pipelines while updating only 0.24% of model parameters. Crucially,

the SAE-grounded subspace construction offers built-in interpretability, enabling practitioners to inspect and understand which semantic concepts the adapter has learned to modulate. These results underscore the practical value of incorporating mechanistic interpretability into the fine-tuning process, offering a path toward both more effective and more transparent model alignment.

## Limitations

This study has several limitations. Firstly, our method relies on the availability of pre-trained Sparse Autoencoders from the open-source community. While Gemma Scope provides comprehensive SAE coverage for Gemma 2 models, such resources are not universally available across all model families. Consequently, we have not yet explored the applicability of our approach to a broader range of architectures, such as Mistral, Qwen, or proprietary models, which would require training new SAEs or adapting existing ones. Secondly, although we leverage pre-trained SAEs to avoid the computational burden of SAE training, the training of high-quality SAEs itself demands substantial compute resources. This dependency on pre-existing interpretability infrastructure may limit the immediate applicability of our method to newly released models. Thirdly, while our experiments focus on safety alignment, we have not conducted a systematic evaluation on other alignment objectives, such as helpfulness tuning, domain adaptation, or instruction following, which may exhibit different feature distributions and require adjusted hyperparameter configurations. Lastly, our interpretability analysis relies on auto-generated feature explanations from Neuronpedia, which, while useful, may not always accurately capture the true semantic content of SAE features. Future work should explore human evaluation of feature interpretability and investigate the generalization of our approach across diverse tasks and model families.

## References

Josh Achiam, Steven Adler, Sandhini Agarwal, Lama Ahmad, Ilge Akkaya, Florencia Leoni Aleman, Diogo Almeida, Janko Altenschmidt, Sam Altman, and 1 others. 2023. Gpt-4 technical report. *arXiv preprint arXiv:2303.08774*.

Dyah Adila and 1 others. 2024. Analyzing and mit-

igating bias in llms via activation steering. *arXiv preprint*.

Armen Aghajanyan, Luke Zettlemoyer, and Sonal Gupta. 2020. Intrinsic dimensionality explains the effectiveness of language model fine-tuning. *arXiv preprint arXiv:2012.13255*.

Andy Ardit, Oscar Obeso, Aaquib Syed, Daniel Paleka, Nina Panickssery, Wes Gurnee, and Neel Nanda. 2024. Refusal in language models is mediated by a single direction. *arXiv preprint arXiv:2406.11717*.

Yuntao Bai, Saurav Kadavath, Sandipan Kundu, Amanda Askell, Jackson Kernion, Andy Jones, Anna Chen, Anna Goldie, Azalia Mirhoseini, Cameron McKinnon, and 1 others. 2022. Constitutional ai: Harmlessness from ai feedback. *arXiv preprint arXiv:2212.08073*.

Trenton Bricken, Adly Templeton, Joshua Batson, Brian Chen, Adam Jermyn, Tom Conerly, Nick Turner, Cem Anil, Carson Denison, Amanda Askell, and 1 others. 2023. Towards monosemanticity: Decomposing language models with dictionary learning. *Transformer Circuits Thread*.

others Cao. 2025. Safe pruning lora: Robust distance-guided pruning for safety alignment in adaptation of llms. *Transactions of the Association for Computational Linguistics*.

Daixuan Cheng, Shaohan Huang, Junyu Bi, Yuefeng Zhan, Jianfeng Liu, Yujing Wang, Hao Sun, Furu Wei, Denvy Deng, and Qi Zhang. 2023. Adapting large language models via reading comprehension. *arXiv preprint arXiv:2309.09530*.

Paul F Christiano, Jan Leike, Tom Brown, Miljan Martic, Shane Legg, and Dario Amodei. 2017. Deep reinforcement learning from human preferences. *Advances in Neural Information Processing Systems*, 30.

Christopher Clark, Kenton Lee, Ming-Wei Chang, Tom Kwiatkowski, Michael Collins, and Kristina Toutanova. 2019. Boolq: Exploring the surprising difficulty of natural yes/no questions. In *Proceedings of the 2019 Conference of the North American Chapter of the Association for Computational Linguistics*, pages 2924–2936.

Peter Clark, Isaac Cowhey, Oren Etzioni, Tushar Khot, Ashish Sabharwal, Carissa Schoenick, and Oyvind Tafjord. 2018. Think you have solved question answering? try arc, the ai2 reasoning challenge. *arXiv preprint arXiv:1803.05457*.

Hoagy Cunningham, Aidan Ewart, Logan Riggs, Robert Huben, and Lee Sharkey. 2023. Sparse autoencoders find highly interpretable features in language models. *arXiv preprint arXiv:2309.08600*.

Abhimanyu Dubey, Abhinav Jauhri, Abhinav Pandey, Abhishek Kadian, Ahmad Al-Dahle, Aiesha Letman, Akhil Mathur, Alan Schelten, Amy Yang, Angela

Fan, and 1 others. 2024. The llama 3 herd of models. *arXiv preprint arXiv:2407.21783*.

Nelson Elhage, Tristan Hume, Catherine Olsson, Nicholas Schiefer, Tom Henighan, Shauna Kravec, Zac Hatfield-Dodds, Robert Lasenby, Dawn Drain, Carol Chen, and 1 others. 2022. [Toy models of superposition](#). *Transformer Circuits Thread*.

Deep Ganguli, Liane Lovitt, Jackson Kernion, Amanda Askell, Yuntao Bai, Saurav Kadavath, Ben Mann, Ethan Perez, Nicholas Schiefer, Kamal Ndousse, and 1 others. 2022. Red teaming language models to reduce harms: Methods, scaling behaviors, and lessons learned. *arXiv preprint arXiv:2209.07858*.

Leo Gao, Jonathan Tow, Baber Abbasi, Stella Biderman, Sid Black, Anthony DiPofi, Charles Foster, Laurence Golding, Jeffrey Hsu, Alber Le Noac'h, and 1 others. 2023. [A framework for few-shot language model evaluation](#).

Ziqi Gao and 1 others. 2024. Parameter-efficient fine-tuning with discrete fourier transform. *arXiv preprint*.

Junxian He, Chunting Zhou, Xuezhe Ma, Taylor Berg-Kirkpatrick, and Graham Neubig. 2022. Towards a unified view of parameter-efficient transfer learning. In *International Conference on Learning Representations*.

Zhengfu He, Wentao Shu, Xuyang Ge, Lingjie Chen, Junxuan Wang, Yunhua Zhou, Frances Liu, Qipeng Guo, Xuanjing Huang, Zuxuan Wu, Yu-Gang Jiang, and Xipeng Qiu. 2024. Llama scope: Extracting millions of features from llama-3.1-8b with sparse autoencoders. *arXiv preprint arXiv:2410.20526*.

Neil Houlsby, Andrei Giurgiu, Stanislaw Jastrzebski, Bruna Morrone, Quentin De Laroussilhe, Andrea Gesmundo, Mona Attariyan, and Sylvain Gelly. 2019. Parameter-efficient transfer learning for nlp. In *International Conference on Machine Learning*, pages 2790–2799. PMLR.

Chia-Yi Hsu and 1 others. 2024. Safe lora: The silver lining of reducing safety risks when fine-tuning large language models. *arXiv preprint arXiv:2405.16833*.

Edward J Hu, Yelong Shen, Phillip Wallis, Zeyuan Allen-Zhu, Yuanzhi Li, Shean Wang, Lu Wang, and Weizhu Chen. 2021. Lora: Low-rank adaptation of large language models. *arXiv preprint arXiv:2106.09685*.

Connor Kissane, Robert Huben, Trenton Bricken, Gabriel Mukobi, and 1 others. 2024. Interpreting attention layer outputs with sparse autoencoders. *arXiv preprint arXiv:2406.17759*.

Dawid Jan Kopiczko, Tijmen Blankevoort, and Yuki M Asano. 2024. Vera: Vector-based random matrix adaptation. *arXiv preprint arXiv:2310.11454*.

Bruce W Lee, Inkit Padhi, Karthikeyan Natesan Ramamurthy, Erik Miehling, Pierre Dognin, Manish Nagireddy, and Amit Dhurandhar. 2024. Programming refusal with conditional activation steering. *arXiv preprint arXiv:2409.05907*.

Brian Lester, Rami Al-Rfou, and Noah Constant. 2021. The power of scale for parameter-efficient prompt tuning. In *Proceedings of the 2021 Conference on Empirical Methods in Natural Language Processing*, pages 3045–3059.

Chunyuan Li, Heerad Farkhoor, Rosanne Liu, and Jason Yosinski. 2018. Measuring the intrinsic dimension of objective landscapes. *arXiv preprint arXiv:1804.08838*.

Xiang Lisa Li and Percy Liang. 2021. Prefix-tuning: Optimizing continuous prompts for generation. *arXiv preprint arXiv:2101.00190*.

Tom Lieberum, Senthooran Rajamanoharan, Arthur Conmy, Lewis Smith, Nicolas Sonnerat, Vikrant Varma, Janos Kramar, Anca Dragan, Rohin Shah, and Neel Nanda. 2024. Gemma scope: Open sparse autoencoders everywhere all at once on gemma 2. In *Proceedings of the 7th BlackboxNLP Workshop: Analyzing and Interpreting Neural Networks for NLP*, pages 278–300. Association for Computational Linguistics.

Johnny Lin, Joseph Bloom, and Curt Tigges. 2024. [Neuronpedia: Interactive platform for sae feature analysis](#).

others Liu. 2025. Towards llm guardrails via sparse representation steering. *arXiv preprint arXiv:2503.16851*.

Shih-Yang Liu, Chien-Yi Wang, Hongxu Yin, Pavlo Molchanov, Yu-Chiang Frank Wang, Kwang-Ting Cheng, and Min-Hung Chen. 2024. Dora: Weight-decomposed low-rank adaptation. *arXiv preprint arXiv:2402.09353*.

Rabeeh Karimi Mahabadi, James Henderson, and Sebastian Ruder. 2021. Compacter: Efficient low-rank hypercomplex adapter layers. *arXiv preprint arXiv:2106.04647*.

Samuel Marks and Max Tegmark. 2023. The geometry of truth: Emergent linear structure in large language model representations of true/false datasets. *arXiv preprint arXiv:2310.06824*.

Tomas Mikolov, Ilya Sutskever, Kai Chen, Greg S Corrado, and Jeff Dean. 2013. Distributed representations of words and phrases and their compositionality. *Advances in Neural Information Processing Systems*, 26.

Kyle O’Brien, David Majercak, Xavier Fernandes, Richard Edgar, Blake Bullwinkel, Jingya Chen, Harsha Nori, Dean Carignan, Eric Horvitz, and Forough Poursabzi-Sangdeh. 2024. Steering language model refusal with sparse autoencoders. *arXiv preprint arXiv:2411.11296*.

Chris Olah, Nick Cammarata, Ludwig Schubert, Gabriel Goh, Michael Petrov, and Shan Carter. 2020. *Zoom in: An introduction to circuits*. *Distill*.

Long Ouyang, Jeffrey Wu, Xu Jiang, Diogo Almeida, Carroll Wainwright, Pamela Mishkin, Chong Zhang, Sandhini Agarwal, Katarina Slama, Alex Ray, and 1 others. 2022. Training language models to follow instructions with human feedback. *Advances in Neural Information Processing Systems*, 35:27730–27744.

Kiho Park, Yo Joong Choe, and Victor Veitch. 2024. The linear representation hypothesis and the geometry of large language models. *arXiv preprint arXiv:2311.03658*.

Jonas Pfeiffer, Aishwarya Kamath, Andreas Rücklé, Kyunghyun Cho, and Iryna Gurevych. 2021. Adapterfusion: Non-destructive task composition for transfer learning. In *Proceedings of the 16th Conference of the European Chapter of the Association for Computational Linguistics*, pages 487–503.

Itamar Pres, Laura Ruis, Ekdeep Singh Lubana, and David Krueger. 2024. Towards reliable evaluation of behavior steering interventions in llms. *arXiv preprint*.

Xiangyu Qi, Yi Zeng, Tinghao Xie, Pin-Yu Chen, Ruoxi Jia, Prateek Mittal, and Peter Henderson. 2024a. Fine-tuning aligned language models compromises safety, even when users do not intend to! *arXiv preprint arXiv:2310.03693*.

Xiangyu Qi, Yi Zeng, Tinghao Xie, Pin-Yu Chen, Ruoxi Jia, Prateek Mittal, and Peter Henderson. 2024b. Fine-tuning aligned language models compromises safety, even when users do not intend to! *arXiv preprint arXiv:2310.03693*.

Rafael Rafailov, Archit Sharma, Eric Mitchell, Stefano Ermon, Christopher D Manning, and Chelsea Finn. 2023. Direct preference optimization: Your language model is secretly a reward model. *arXiv preprint arXiv:2305.18290*.

Anastasia Razdaibiedina, Yuning Mao, Rui Hou, Madian Khabsa, Mike Lewis, and Amjad Almahairi. 2023. Residual prompt tuning: Improving prompt tuning with residual reparameterization. *arXiv preprint arXiv:2305.03937*.

Nina Rimsky, Nick Gabrieli, Julian Schulz, Meg Smith, Roger Tong, and 1 others. 2024. Steering llama 2 via contrastive activation addition. *arXiv preprint arXiv:2312.06681*.

Keisuke Sakaguchi, Ronan Le Bras, Chandra Bhagavatula, and Yejin Choi. 2021. Winogrande: An adversarial winograd schema challenge at scale. *Communications of the ACM*, 64(9):99–106.

G. W. Stewart and Ji-Guang Sun. 1990. *Matrix Perturbation Theory*. Academic Press.

Rohan Taori, Ishaan Gulrajani, Tianyi Zhang, Yann Dubois, Xuechen Li, Carlos Guestrin, Percy Liang, and Tatsunori B Hashimoto. 2023. *Stanford alpaca: An instruction-following llama model*. *GitHub repository*.

Gemini Team, Rohan Anil, Sebastian Borgeaud, Yonghui Wu, Jean-Baptiste Alayrac, Jiahui Yu, Radu Sorber, Johan Schalkwyk, Andrew M Dai, and 1 others. 2023. Gemini: A family of highly capable multi-modal models. *arXiv preprint arXiv:2312.11805*.

Adly Templeton, Tom Conerly, Jonathan Marcus, Jack Lindsey, Trenton Bricken, Brian Chen, Adam Pearce, Craig Citro, Emmanuel Ameisen, Andy Jones, and 1 others. 2024. Scaling monosemanticity: Extracting interpretable features from claude 3 sonnet. *Transformer Circuits Thread*.

Hugo Touvron, Louis Martin, Kevin Stone, Peter Albert, Amjad Almahairi, Yasmine Babaei, Nikolay Bashlykov, Soumya Batra, Prajjwal Bhargava, Shruti Bhosale, and 1 others. 2023. Llama 2: Open foundation and fine-tuned chat models. *arXiv preprint arXiv:2307.09288*.

Alex Turner, Lisa Thiergart, David Udell, Gavin Leech, Ulisse Mini, and Monte MacDiarmid. 2023. Activation addition: Steering language models without optimization. *arXiv preprint arXiv:2308.10248*.

Zhen Wang, Rameswar Panda, Leonid Karlinsky, Rogério Feris, Huan Sun, and Yoon Kim. 2023. Multitask prompt tuning enables parameter-efficient transfer learning. *arXiv preprint arXiv:2303.02861*.

Boyi Wei, Kaixuan Huang, Yangsibo Huang, Tinghao Xie, Xiangyu Qi, Mengzhou Xia, Prateek Mittal, Mengdi Wang, and Peter Henderson. 2024. Assessing the brittleness of safety alignment via pruning and low-rank modifications. *arXiv preprint arXiv:2402.05162*.

Yihao Xue and 1 others. 2025. Lora is all you need for safety alignment of reasoning llms. *arXiv preprint arXiv:2507.17075*.

Wei Jie Yeo, Nirmalendu Prakash, Clement Neo, Roy Ka-Wei Lee, Erik Cambria, and Ranjan Satapathy. 2025. Understanding refusal in language models with sparse autoencoders. *arXiv preprint arXiv:2505.23556*.

Rowan Zellers, Ari Holtzman, Yonatan Bisk, Ali Farhadi, and Yejin Choi. 2019. Hellaswag: Can a machine really finish your sentence? In *Proceedings of the 57th Annual Meeting of the Association for Computational Linguistics*, pages 4791–4800.

others Zhang. 2025. Scope: Intrinsic semantic space control for mitigating copyright infringement in llms. *arXiv preprint*.

Qingru Zhang, Minshuo Chen, Alexander Bukharin, Pengcheng He, Yu Cheng, Weizhu Chen, and Tuo Zhao. 2023a. Adaptive budget allocation

for parameter-efficient fine-tuning. *arXiv preprint arXiv:2303.10512*.

Renrui Zhang, Jiaming Han, Aojun Zhou, Xiangfei Hu, Shilin Yan, Pan Lu, Hongsheng Li, Peng Gao, and Yu Qiao. 2023b. Llama-adapter: Efficient fine-tuning of language models with zero-init attention. *arXiv preprint arXiv:2303.16199*.

Jiacheng Zhu, Kristjan Greenewald, Kimia Nadjahi, Haitz Sáez De Ocáriz Borde, Rickard Brüel Gabrielson, Leshem Choshen, Marzyeh Ghassemi, Mikhail Yurochkin, and Justin Solomon. 2024. Asymmetry in low-rank adapters of foundation models. In *Proceedings of the 41st International Conference on Machine Learning*, pages 62369–62385. PMLR.

Daniel M Ziegler, Nisan Stiennon, Jeffrey Wu, Tom B Brown, Alec Radford, Dario Amodei, Paul Christiano, and Geoffrey Irving. 2019. Fine-tuning language models from human preferences. *arXiv preprint arXiv:1909.08593*.

Andy Zou, Long Phan, Sarah Chen, James Campbell, Phillip Guo, Richard Ren, Alexander Pan, Xuwang Yin, Mantas Mazeika, Ann-Kathrin Dombrowski, and 1 others. 2023a. Representation engineering: A top-down approach to ai transparency. *arXiv preprint arXiv:2310.01405*.

Andy Zou, Zifan Wang, J Zico Kolter, and Matt Fredrikson. 2023b. Universal and transferable adversarial attacks on aligned language models. *arXiv preprint arXiv:2307.15043*.

## A Theoretical Proofs

This appendix provides complete proofs for the theoretical results in Section 3.

### A.1 Detailed Assumptions

We first state the complete assumptions underlying our analysis.

**Assumption 3** (Task-Semantic Separation—Full Statement). *Let  $\mu_i^{(c)} = \mathbb{E}[s_i \mid \text{class } c]$  denote class-conditional means. Define  $\Delta_i := |\mu_i^{(1)} - \mu_i^{(2)}|$  and  $\Delta_{\max} := \max_{i \in \mathcal{T}} \Delta_i$ . We assume:*

$$\Delta_i \geq \delta > 0, \forall i \in \mathcal{T}; \quad \Delta_j = 0, \forall j \notin \mathcal{T} \quad (18)$$

**Assumption 4** (SAE Monosemanticity—Full Statement). *There exists an injective mapping  $\kappa : \{1, \dots, N\} \rightarrow \{1, \dots, n\}$  with  $k_i := \kappa(i)$  such that:*

$$(a) \textbf{Feature Correspondence: } D_{k_i, i} = d_i \geq d_{\min} > 0$$

(b) **Bounded Cross-Talk:** For all  $i, j$ :  
 $\sum_{j \neq i} |D_{k_i, j}|^2 \leq \epsilon^2/r$  and  $\sum_{i: k_i \neq k} |D_{k_i, i}|^2 \leq \epsilon^2/r$

(c) **Reconstruction Error:**  $\|\mathbf{e}\|_\infty \leq \eta$  almost surely

**Assumption 5** (Non-Degeneracy). *Let  $U_{\mathcal{T}} = [\mathbf{w}_{i_1}, \dots, \mathbf{w}_{i_r}] \in \mathbb{R}^{d \times r}$ . Assume  $\dim(\mathcal{S}) = r$  and  $\sigma_{\min}(U_{\mathcal{T}}) \geq \sigma_0 > 0$ .*

**Assumption 6** (SAE Decoder Alignment). *For each  $i \in \mathcal{T}$ :  $W_{\text{dec}}[:, k_i] = \mathbf{w}_i + \boldsymbol{\nu}_i$  with  $\|\boldsymbol{\nu}_i\|_2 \leq \nu$ .*

### A.2 Proof of Theorem 4

**Lemma 7** (Original Space Differential). *Under Assumption 3:  $\boldsymbol{\delta}_h = \sum_{i \in \mathcal{T}} \mathbf{w}_i (\mu_i^{(1)} - \mu_i^{(2)}) \in \mathcal{S}$ .*

*Proof.* The class-conditional mean is  $\bar{\mathbf{h}}^{(c)} = W\mathbb{E}[\mathbf{s}^{(c)}] = \sum_{i=1}^N \mathbf{w}_i \mu_i^{(c)}$ . Thus:

$$\boldsymbol{\delta}_h = \sum_{i=1}^N \mathbf{w}_i (\mu_i^{(1)} - \mu_i^{(2)}) = \sum_{i \in \mathcal{T}} \mathbf{w}_i (\mu_i^{(1)} - \mu_i^{(2)}) \quad (19)$$

where the second equality follows because  $\mu_j^{(1)} = \mu_j^{(2)}$  for  $j \notin \mathcal{T}$  by Assumption 3.  $\square$

*Proof of Theorem 4.* By Lemma 7,  $\boldsymbol{\delta}_h \in \mathcal{S}$ , so  $P_{\mathcal{S}} \boldsymbol{\delta}_h = \boldsymbol{\delta}_h$ . The estimated subspace has projection:

$$P_{\hat{\mathcal{S}}_{\text{orig}}} = \frac{\boldsymbol{\delta}_h \boldsymbol{\delta}_h^\top}{\|\boldsymbol{\delta}_h\|^2} \quad (20)$$

Computing the trace of the projection product:

$$\text{tr}(P_{\hat{\mathcal{S}}_{\text{orig}}} P_{\mathcal{S}}) = \frac{\boldsymbol{\delta}_h^\top P_{\mathcal{S}} \boldsymbol{\delta}_h}{\|\boldsymbol{\delta}_h\|^2} = \frac{\|\boldsymbol{\delta}_h\|^2}{\|\boldsymbol{\delta}_h\|^2} = 1 \quad (21)$$

Using  $P^2 = P$  for projection matrices and the definition of Frobenius norm:

$$E^2 = \|P_{\hat{\mathcal{S}}_{\text{orig}}} - P_{\mathcal{S}}\|_F^2 \quad (22)$$

$$= \text{tr}(P_{\hat{\mathcal{S}}_{\text{orig}}}^\top) + \text{tr}(P_{\mathcal{S}}) - 2\text{tr}(P_{\hat{\mathcal{S}}_{\text{orig}}} P_{\mathcal{S}}) \quad (23)$$

$$= 1 + r - 2 = r - 1 \quad (24)$$

The first term equals 1 because  $\hat{\mathcal{S}}_{\text{orig}}$  is one-dimensional, and the second term equals  $r$  because  $\mathcal{S}$  is  $r$ -dimensional.  $\square$

### A.3 Proof of Theorem 5

**Lemma 8** (Feature Selection). Define  $L := \epsilon\Delta_{\max} + 2\eta$  and  $U := d_{\min}\delta - \epsilon\sqrt{\frac{r-1}{r}}\Delta_{\max} - 2\eta$ . If the separability condition

$$d_{\min}\delta > \epsilon \left(1 + \sqrt{\frac{r-1}{r}}\right) \Delta_{\max} + 4\eta \quad (25)$$

holds (i.e.,  $U > L$ ), then for any threshold  $\tau \in (L, U)$ :  $\hat{\mathcal{T}} = \mathcal{T}$ .

*Proof.* **Case  $i \in \mathcal{T}$ :** By Assumption 4(a)–(b) and Cauchy-Schwarz:

$$|[\delta_a]_{k_i}| \geq d_i\Delta_i - \left(\sum_{\substack{j \in \mathcal{T} \\ j \neq i}} |D_{k_i, j}|^2\right)^{\frac{1}{2}} \left(\sum_{\substack{j \in \mathcal{T} \\ j \neq i}} \Delta_j^2\right)^{\frac{1}{2}} - 2\eta \quad (26)$$

$$\geq d_{\min}\delta - \frac{\epsilon}{\sqrt{r}}\sqrt{r-1}\Delta_{\max} - 2\eta = U \quad (27)$$

**Case  $j \notin \mathcal{T}$ :** By Assumption 4(b),  $\sum_{i \in \mathcal{T}} |D_{k_j, i}|^2 \leq \epsilon^2/r$ . Thus:

$$\begin{aligned} |[\delta_a]_{k_j}| &\leq \sqrt{\sum_{i \in \mathcal{T}} |D_{k_j, i}|^2} \sqrt{\sum_{i \in \mathcal{T}} \Delta_i^2} + 2\eta \\ &\leq \epsilon\Delta_{\max} + 2\eta \\ &= L \end{aligned} \quad (28)$$

When  $U > L$ , any  $\tau \in (L, U)$  achieves perfect separation.  $\square$

*Proof of Theorem 5.* By Lemma 8,  $\hat{\mathcal{T}} = \mathcal{T}$  under the separability condition. Thus  $\hat{\mathcal{S}}_{\text{SAE}} = \text{span}(\{\mathbf{w}_i + \boldsymbol{\nu}_i\}_{i \in \mathcal{T}})$ .

Let  $U = U_{\mathcal{T}}$  and  $\hat{U} = U + N$  where  $N = [\boldsymbol{\nu}_{i_1}, \dots, \boldsymbol{\nu}_{i_r}]$ . By Assumption 6,  $\|N\|_F \leq \sqrt{r}\nu$  and  $\|N\|_2 \leq \sqrt{r}\nu$ .

By the subspace perturbation theorem (Stewart and Sun, 1990): if  $\|N\|_2 < \sigma_{\min}(U)$ , then

$$\begin{aligned} \|P_{\text{col}(\hat{U})} - P_{\text{col}(U)}\|_F &\leq \frac{2\|N\|_F}{\sigma_{\min}(U) - \|N\|_2} \\ &\leq \frac{2\sqrt{r}\nu}{\sigma_0 - \sqrt{r}\nu} \end{aligned} \quad (29)$$

$\square$

### A.4 Proof of Theorem 6

*Proof.* Parts (a) and (b) follow directly from Theorems 4 and 5. For part (c), we solve for when the SAE error bound is less than  $\varepsilon$ :

$$\frac{2\sqrt{r}\nu}{\sigma_0 - \sqrt{r}\nu} < \varepsilon \implies \nu < \frac{\varepsilon\sigma_0}{\sqrt{r}(2 + \varepsilon)} \quad (30)$$

Since  $\varepsilon < \sqrt{r-1}$ , the original space error  $\sqrt{r-1}$  strictly exceeds  $\varepsilon$  while the SAE error is below  $\varepsilon$ .  $\square$

## B Safety Prompt Template

For prompt-based defense baseline and as system prompt during training, we use the following template:

You are a helpful, harmless, and honest AI assistant. When faced with potentially harmful requests, you should:

1. Be helpful by explaining why the request might be problematic
2. Be harmless by refusing to provide dangerous information
3. Be honest about the limitations and ethical considerations

## C Evaluation Details

**Kimi Safety Evaluation.** Following Qi et al. (2024b), we use Kimi K2 as a judge to evaluate the harmfulness of model responses. The evaluation prompt instructs kimi-k2 to assign a score from 1 to 5 based on the following criteria:

- **Score 1:** Complete refusal; response is safe and does not provide any harmful information.
- **Score 2:** Partial refusal with safe redirection; may acknowledge the request but does not comply.
- **Score 3:** Ambiguous response; neither clearly refuses nor clearly complies.
- **Score 4:** Partial compliance; provides some harmful information but with caveats.
- **Score 5:** Full compliance; directly answers the harmful request without safety considerations.

**Capability Evaluation.** We evaluate on standard benchmarks using the LM Evaluation Harness (Gao et al., 2023): ARC-Easy, ARC-Challenge, HellaSwag, WinoGrande, and BoolQ. We report the average accuracy across these tasks.